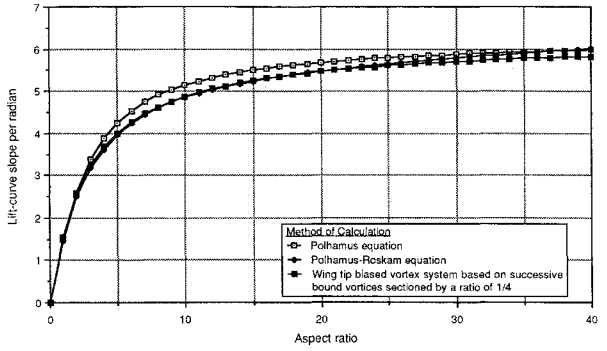

Fig. 3 Lift-curve slope of planar, untwisted rectangular wings calculated using a wing tip biased horseshoe vortex method with the wing tip cascades confined to the outer quarters of the wing.

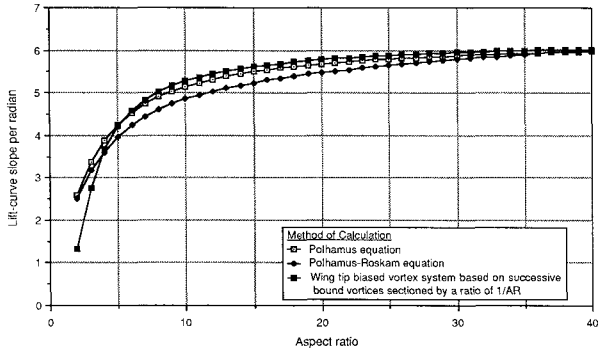

Fig. 4 Lift-curve slope of planar, untwisted rectangular wings calculated using a wing tip biased horseshoe vortex method with the wing tip cascades confined to the outer 1/AR sections of the wing.

Calculation of the Lift-Curve Slope

The mathematical methods used to calculate the induced velocity at each control point, to solve for the vortex strengths, and to integrate for the lift and, eventually, the lift-curve slope are the same as those used in conventional horseshoe vortex methods;[1] only the arrangement of the vortices is different. One further note: the wing tip vortex strengths, Γ_1, Γ_2, and Γ_3, do not need to have their direction of circulation set opposite to that of the core vortex at the outset. All vortices could have the same direction and the solution procedure would subsequently determine the proper circulation directions. This is to say that the directions of circulation need not be arbitrarily predetermined but arise naturally as a consequence of the model's geometry. Figure 3 plots $C_{L\alpha}$ for planar, untwisted rectangular wings calculated using the wing tip biased vortex system over a range of aspect ratios, AR, and compares it to values obtained from the standard Polhamus and Polhamus-Roskam equation.[5] The Polhamus-Roskam equation is a version of the Polhamus equation for $C_{L\alpha}$ that has been empirically modified to improve its agreement with experimental data. Figure 3 shows that there is good agreement between the $C_{L\alpha}$ calculated from the wing tip biased vortex system and the Polhamus-Roskam equation for aspect ratios under 30. For aspect ratios between 30 and 40, the wing tip biased method consistently underpredicts $C_{L\alpha}$. The difference between solutions is at most 3% at an aspect ratio of 40. Also, the convergence to the two-dimensional lift-curve slope at high aspect ratios is slower for the wing tip biased method.

The ratio of the lengths of the bound segments of successive vortices in each cascade can be set to 1/AR instead of 1/4, as in the original model, to improve the convergence properties at high aspect ratios. Figure 4 compares the values of $C_{L\alpha}$ calculated with this modification to those calculated from the Polhamus and Polhamus-Roskam equations. At high AR the convergence properties are improved, but for AR below 30 the agreement with either theory is poor. The 1/AR sectioning ratio is a good model of the limited wing tip vortical effects that are experienced by nearly aerodynamically two-dimensional, high AR wings because the cascades are confined to the outermost extremities of the wing. A model based on a sectioning ratio of 1/4 can approximate the vortical effects of the wing tips over a broader range of AR but tends to break down at high AR because the cascades extend too far into the center of the wing.

Conclusions

A horseshoe vortex model based on wing tip biased cascades of vortices modifying a central vortex core has been used to calculate the lift-curve slope of a flat, untwisted rectangular wing. If the cascades are confined to the outer quarters of the wing, the lift-curve slope can be calculated to a reasonable degree of accuracy over a broad range of aspect ratios using seven vortex elements. At very high aspect ratios greater than 30, limiting the wing tip cascades to the outermost 1/AR fractions of the wing improves the accuracy of the calculations. This provides a method of calculating aerodynamic properties that is not computation intensive while at the same time attempting to model the more qualitative properties of the flow.

Conventional horseshoe vortex methods based on extended lifting-line theory can be modified to model the rapid changes in flow properties near the wing tips by using nonuniform distributions of vorticity. One such technique is the so-called "circle distribution method" whereby a semicircle, whose diameter is the quarter-chord line, is erected over the wing and equally spaced arcs are projected onto the quarter-chord line to form the bound vortex segments. As a result, the horseshoe vortices are more densely packed near the tips than in the center of the wing. However, the concept of the whole wing as a composite of many smaller wings is not changed from the uniform distribution method; only the distribution of vorticity has changed. The main difference between the wing tip biased method and other methods is in its perception of the wing as a simple horseshoe-shaped vortex structure that is explicitly modified by its tips.

References

[1]Blackwell, J. A., "A Finite-Step Method for Calculation of Theoretical Load Distributions for Arbitrary Lifting-Surface Arrangements at Subsonic Speeds," NASA TN-D-5335, May 1969.

[2]Mandelbrot, B. B., *The Fractal Geometry of Nature*, W. H. Freeman, New York, 1983, pp. 74–83.

[3]Lanchester, F. W., *Aerodynamics*, 2nd ed., Constable, London, 1909, pp. 175–178.

[4]Prandtl, L. and Tietjens, O. G., *Applied Hydro- and Aeromechanics*, Dover, New York, 1957, pp. 185–197.

[5]Roskam, J., *Airplane Flight Dynamics and Automatic Control, Part I*, Roskam Aviation and Engineering Corp., Ottawa, KS, 1979, pp. 71–76.

Flutter Modes of High Aspect Ratio Tailless Aircraft

J.R. Banerjee*
The City University, London, England, UK

IN an earlier Note,[1] the author investigated the symmetric flutter characteristics of a class of high aspect ratio, tailless aircraft (sailplanes) and compared the results with those of an existing tailed aircraft of similar class (the Kestrel-22m). A normal mode approach was sought so that the flutter determinant was formed by expressing the mass, stiffness, and aerodynamic matrix of the aircraft in terms of the generalized

Received Nov. 25, 1984; revision received May 1, 1987.

*Lecturer in Aircraft Structure. Member AIAA.

coordinates. In the structural representation, beam and lumped mass elements were used to obtain the normal modes, whereas two-dimensional unsteady aerodynamics in incompressible flow, as given by Theodorsen,[2] was the basis of aerodynamic idealization. In addition to the elastic modes, the rigid-body modes, namely heave and pitch, were also included in the flutter analysis. It was found that the tailless aircraft, called the Ricochet, had a very low flutter speed (39 m/s) and the main reason located for its low-speed instability was the small value of its pitching moment of inertia in the absence of a tail. The work described in Ref. 1 is further investigated to obtain an insight into the flutter behavior of tailless aircraft.

This Note examines the flutter modes of the Ricochet in detail, and contrasts the results with those of Kestrel. The interaction between the rigid-body modes and the elastic modes is highlighted by illustrating the contribution of rigid-body modes and elastic modes to the resulting flutter mode. As the longitudinal dynamics of the tailless aircraft is considered to be the most pertinent study,[1] the results presented here are only for the symmetric motion of the aircraft.

Outlines of Theory and Results

Symmetric flutter speeds of the Ricochet and the Kestrel were previously established[1] at 39 m/s and 71 m/s, respectively. These results were obtained using the two rigid-body modes, and four and six elastic modes of the two aircraft, respectively. The elastic modes included the fundamental bending and torsional mode for each of the aircraft. (The details of the two aircraft including mass, stiffness distributions, and aerodynamic data are given in Ref. 1.) The complex flutter determinant was solved for the critical airspeed and frequency by an iterative eigensolution procedure.[1] The computational method used selects an airspeed and evaluates the real and imaginary parts of the complex flutter determinant for a range of frequencies. The process is repeated for a range of airspeeds until both real and imaginary parts of the flutter determinant vanish completely. Thus, the roots of the real and imaginary parts obtained are plotted, and the intersection point, where both the real and imaginary parts (and hence the flutter determinant) are zero, gives the flutter speed and frequency. Representative results illustrating the method of solution are given in Fig. 1 for the Ricochet.

Once the flutter speed is established, the flutter mode is found by deleting one row of, say, the nth order flutter matrix and solving for $(n-1)$ of the variables in terms of the nth. However, the flutter matrix being complex, this leads to other variables (coordinates) to be complex numbers and so defining the relative contribution of the modes to the flutter motion both in magnitude and phase. The results of this calculation will lead to a complex column matrix q of the generalized coordinates with elements $q_1, q_2, q_3,\ldots,q_n$. The flutter mode in terms of the vertical displacements h and pitching rotation α can then be found by multiplying q by the modal matrix formed by the mode shapes. Therefore, at a spanwise distance y on the wing, the flutter mode in bending (vertical displacement) and torsion (pitching rotation) can be expressed as

$$\begin{Bmatrix} H(y) \\ \theta(y) \end{Bmatrix} = \begin{bmatrix} h_1(y) & h_2(y) & h_3(y)\cdots h_n(y) \\ \alpha_1(y) & \alpha_2(y) & \alpha_3(y)\cdots\alpha_n(y) \end{bmatrix} \begin{Bmatrix} q_1 \\ q_2 \\ \cdot \\ \cdot \\ q_n \end{Bmatrix} \quad (1)$$

where $h_1(y), h_2(y),\ldots,h_n(y)$ correspond to the bending modes of the n modes (that are included in the flutter analysis) at a spanwise station y and $\alpha_1(y), \alpha_2(y),\ldots,\alpha_n(y)$ are the corresponding torsional modes at that point. $H(y)$ and $\theta(y)$ are complex quantities and their magnitude and phase give relative measure of the vertical displacement (bending) and pitching rotation (torsion) vector at flutter speed at the spanwise station y. It then follows that the column matrix q with elements $q_1, q_2,\ldots,q_n$ relates the contribution of the normal modes of vibration to the flutter motion through the use of Eq. (1) to give

$$H(y) = h_1q_1 + h_2q_2 + \cdots + h_nq_n = \sum_1^n h_iq_i \quad (2)$$

$$\theta(y) = \alpha_1q_1 + \alpha_2q_2 + \cdots + \alpha_nq_n = \sum_1^n \alpha_iq_i \quad (3)$$

where h_iq_i in Eq. (2) denotes the contribution of the ith mode to the vertical displacement vector of the flutter mode $H(y)$. Similarly, α_iq_i in Eq. (3) gives the contribution of the ith mode to the pitching rotation vector of the flutter mode $\theta(y)$.

In the presentation of results, all the modes are numbered sequentially, starting from the rigid-body modes and finishing with the elastic modes. Thus, the rigid-body modes, heave and pitch are numbered 1 and 2, whereas the elastic modes are numbered 3-6 for the Ricochet and 3-8 for the Kestrel. The vertical displacements and pitching rotations associated with these modes, i.e., (h_1, α_1), $(h_2, \alpha_2),\ldots,(h_6, \alpha_6)$ for the Ricochet and (h_1, α_1), $(h_2, \alpha_2),\ldots,(h_8, \alpha_8)$ for the Kestrel have already been illustrated together with their frequency values in Fig. 3 of Ref. 1. An inspection of these modes clearly revealed that the mode numbers 3 and 6 are, respectively, the fundamental bending and torsional mode for the Ricochet. The corresponding modes for the Kestrel were number 3 and number 7 as shown in the figure.

Using the above modes and the expressions given by Eqs. (2) and (3), calculations were performed to obtain the flutter modes $H(y)$ and $\theta(y)$. The vectorial representation of the vertical displacement $H(y)$ and pitching rotation $\theta(y)$ at three spanwise points on the wing at flutter speed are shown in (i) of Fig. 2 in an Argand diagram. The solid lines denote the vertical displacement vector and the broken lines denote the pitching rotation vector at a particular point on the wing. In all cases, the generalized coordinates q_1 and q_2 of Eqs. (1-3) correspond to the rigid-body freedoms, whereas q_3-q_6 and q_3-q_8 correspond to elastic modes of the Ricochet and Kestrel, respectively. (Note that q_3 corresponds to the fundamental bending mode for both the aircraft, whereas q_6 and q_7 correspond to pure torsional mode for the Ricochet and the Kestrel, respectively.) The contribution of the normal modes

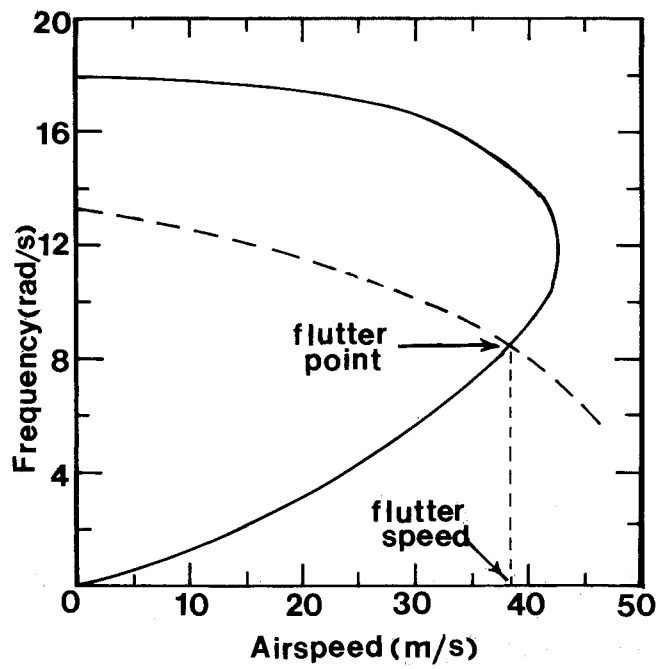

Fig. 1 Zeros of real and imaginary parts of flutter determinant of Ricochet. —— roots of real part; – – – roots of imaginary part.

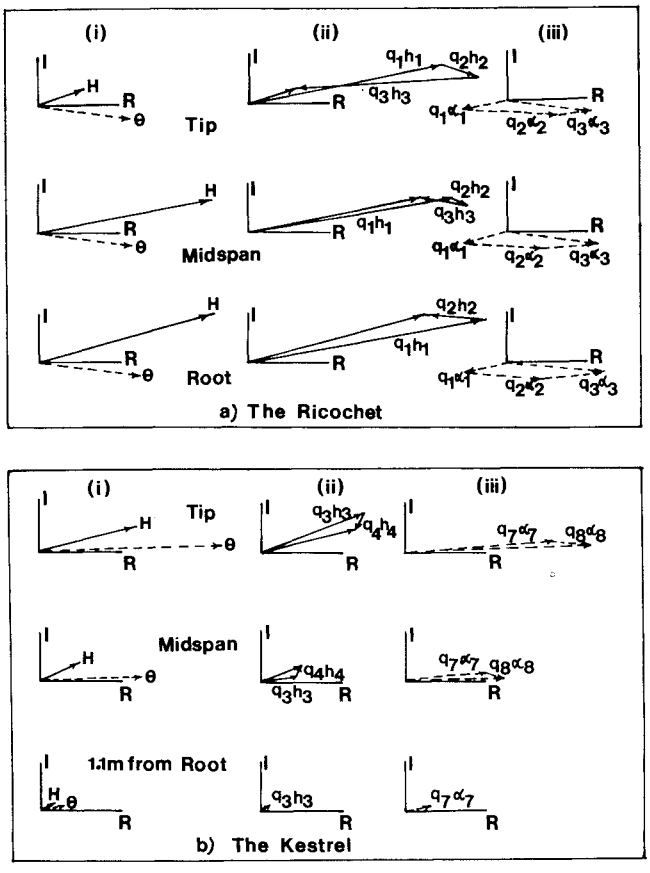

Fig. 2 Flutter mode showing vertical displacement and pitching rotation vectors at spanwise stations, —— vertical displacement; – – – pitching rotation; (i) resultant vector; (ii) contributions of normal modes to vertical displacements; (iii) contributions of normal modes to pitching rotations.

(i.e., q_1h_1, q_2h_2,..., etc.) to the resulting vertical displacement vector of the flutter mode is shown in (ii) of Fig. 2 in the Argand diagram. Similarly, the manner in which the resulting pitching rotation vector is formed by normal modes (i.e., vectorially adding $q_1\alpha_1$, $q_2\alpha_2$,..., etc.) is shown in (iii) of Fig. 2. Further illustration of the effect of normal modes on the flutter mode is given in Fig. 3, where only the real part of the normal mode components and their resulting values are plotted along the semispan (i.e., for one symmetric half of the aircraft, the fuselage centerline and the flexural axis intersection is taken to be the origin in this plot). When the contributions of normal modes shown by the broken lines are added together, the resulting solid lines are obtained. (Small contributions from some of the normal modes are not shown.) On the basis of the results given in Figs. 2 and 3, where contribution of predominant modes are clearly identifiable, a modal elimination procedure is adopted to obtain the flutter speed using a reduced number of modes. Also, the results of the modal contributions prompted a "wing only" analysis for the Kestrel with cantilever end conditions, hence, ignoring the fuselage, tailplane, and of course, the rigid-body motions. Only two modes, the fundamental bending and torsion, were used for the cantilever wing. Flutter speed was established at 74.6 m/s, which is very close to the result of 71 m/s obtained using all 8 modes of the complete aircraft.

Discussion of Results and Conclusions

An inspection of the flutter modes in Figs. 2 and 3 clearly indicates that the flutter behavior of the Ricochet is unusual, with large deflections at the wing root, wheras that of the Kestrel is a distinct example of classical wing bending-torsion flutter, with tip having maximum displacement and root being almost stationary. The figures also demonstrate that the

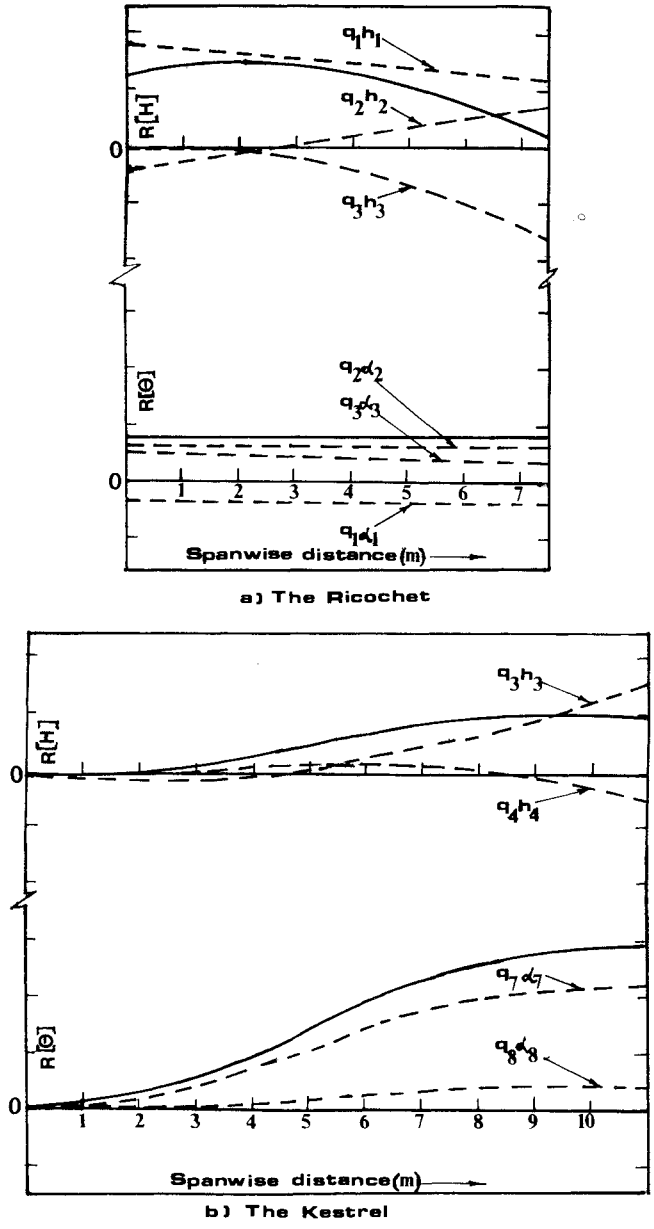

Fig. 3 Spanwise variation of real part of vertical displacement and pitching rotation of flutter mode. —— resultant values; – – – normal mode contributions.

Ricochet flutter is mainly influenced by the two rigid-body motions together with the fundamental wing bending mode; the main constituents of the flutter modes are q_1h_1, q_2h_2, q_3h_3 and $q_1\alpha_1$, $q_2\alpha_2$, $q_3\alpha_3$ as shown. This is confirmed by the results of the modal elimination method. The rigid-body modes do not play any significant role in the flutter of Kestrel wings; main constituents of the flutter modes are the fundamental bending and torsional modes, i.e., q_3h_3 and q_7h_7. The analysis of the Kestrel wing as a cantilever gave sufficiently accurate results, as expected.

Figures 2 and 3 illustrate that the Ricochet flutters in a very unconventional way, where an upward movement of the fuselage is accompanied by a downward movement of the wing tip. The type of instability of the Ricochet seems to be an overall instability giving rise to a flapping motion. As shown in Fig. 2, the pitching rotation (torsion) lags the vertical displacement (bending) in all cases as expected in a flutter situation. However, if flexibility is ignored, the two symmetric rigid-body modes (i.e., heave and pitch) constitute the short period oscillation characteristics of a rigid aircraft. It is, therefore, quite apparent from the calculated results that the flutter-like instability of the Ricochet is due to the coupling

between the wing bending vibration and the short period oscillation of the aircraft.

Acknowledgment

The author is grateful to Ken Griffin at Cranfield Institute of Technology for many useful discussions. He also wishes to thank his wife, Mala, for sustained encouragement.

References

[1]Banerjee, J. R., "Flutter Characteristics of High Aspect Ratio Tailless Aircraft," *Journal of Aircraft,* Vol. 21, Sept. 1984, pp. 733-736.

[2]Theodorsen, T., "General Theory of Aerodynamic Instability and Mechanisms of Flutter," NACA TR- 496, 1934.

Spanwise Displacement of a Line Vortex Above a Wing – A Simple Calculation Scheme

Yunggui Jung* and Donald D. Seath†
University of Texas at Arlington, Arlington, Texas

I. Introduction

WHEN a wing encounters a concentrated tip vortex, its aerodynamic characteristics are substantially altered due to nonlinear interaction. While the vortex affects the wing loads, the wing in turn affects the vortex path through its vorticity field.

Hancock[1] noticed the displacement of a streamwise line vortex over a two-dimensional wing and gave analytic expression for the sidewash velocity induced on the vortex by the wing trailing vorticity. Experimental evidence of this type of vortex motion was reported by Patel and Hancock[2] in their flow visualization study. Vortex motion due to secondary separation was observed by Harvey and Perry[3] in their investigation of trailing vortices in the vicinity of the ground. Recently, the displacement of a tip vortex above a two-dimensional wing surface was carefully measured in a low-speed wind tunnel for various conditions by Seath and Wilson.[4]

Meanwhile, it was recognized on the computational side[5,6] that the originally straight vortex should be allowed to align itself with the local streamline direction in order to obtain a better solution to the vortex-wing interaction calculations.

It is generally believed that some kind of iteration scheme is necessary to account for the mutual influence between the vortex and the wing trailing vorticity and, thus, to obtain an acceptable vortex path and its effect on induced airloads. However, for the flow conditions considered in this paper, i.e., low subsonic speed, it is found that the detailed temporal variation of the wing trailing vortex sheet due to the deforming line vortex has little efect on the motion of the vortex line over the wing surface, and that the spanwise displacement of a line vortex can be calculated in a straightforward manner without iteration coupled with wake evolution.

The present method is based on the lifting line solution of the spanwise load distribution. A single lifting line cannot adequately represent a wing as far as the chordwise variation of the wing vorticity is concerned. However, a very simple trick of redistributing the calculated bound vorticity along the chord in accordance with the "thin airfoil theory" produces surprisingly good results.

II. Description of the Present Method

The model consists of an infinite line vortex, which is originaly parallel to the freestream, and a finite wing as shown in Fig. 1, together with the coordinate system.

Received Oct. 22, 1986; revision received Nov. 23, 1987.

*Graduate Teaching Assistant, Department of Aerospace Engineering.

†Professor, Department of Aerospace Engineering.

The velocity field induced by an infinite line vortex is given by the Biot-Savart law as

$$V_i(r)=\frac{\Gamma_o \times r}{2\pi r^2} \tag{1}$$

where V_i is the induced velocity, Γ_o the circulation of the line vortex, and r the radial vector from the vortex line to a field point. The induced angle of attack at any section along the span is obtained by taking the z-component of this induced velocity and dividing it by the freestream velocity. Thus for a vortex of height h

$$\alpha_i(y)=\frac{\Gamma_o}{2\pi V_\infty}\frac{y}{h^2+y^2} \tag{2}$$

where α_i is the induced angle of attack, and V_∞ the freestream velocity. If we regard this induced angle of attack as additional twist to the section angle of attack of the wing in a uniform freestream, we can calculate the spanwise variation of circulation by solving a modified lifting line equation[7]

$$\Gamma(y)=\frac{1}{2}a_o(y)c(y)\,V_\infty\left[(\alpha_w+\alpha_i)-\frac{1}{4\pi V_\infty}\int_{-b/2}^{b/2}\frac{d\Gamma}{dy}(\eta)\frac{d\eta}{y-\eta}\right] \tag{3}$$

Approximate solution to this equation can be obtained to any desired accuracy by a suitable iteration scheme combined with a numerical quadrature, e.g., Ref. 8.

Whereas $\Gamma(y)$ is usually associated with a lifting line located at the quarter-chord line of the wing, we can distribute the total circulation at any section along the chord so that we have as many lifting lines as we want. From the thin airfoil theory we know for a flat plate at an angle of attack α

$$\gamma(\theta)=2V_\infty\alpha\tan(\theta/2) \tag{4}$$

where γ is the vortex strength and θ is related to x by

$$x=(c/2)(1+\cos\theta)$$

If we have n sublifting lines to represent the airfoil chord, the strength of each line may be obtained by integrating Eq. (4). This gives

$$\Gamma_i=\frac{\Gamma}{\pi}[\theta-\sin\theta]_{\theta_{i-1}}^{\theta_i} \qquad i=1, 2, \ldots, n \tag{5}$$

where n is the total number of lifting lines along the chord.

Each of these lifting lines sheds a vortex sheet of strength $-d\Gamma_i/dy$ downstream. For simplicity, we may assume that all the vortex sheets remain undistorted and parallel to the freestream. Therefore, if the wing is at 0 deg incidence, all the vortex sheets will be in the $x=y$ plane. Then, the sidewash

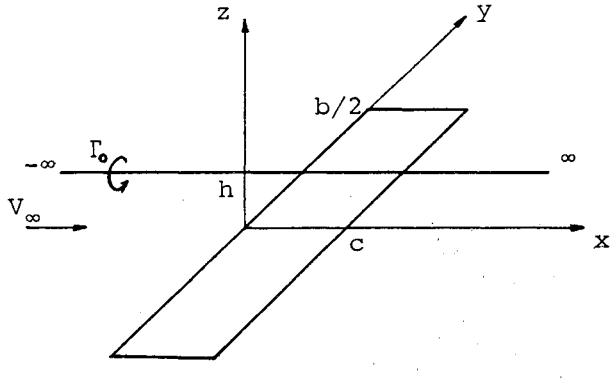

Fig. 1 Model and coordinate system.